Modeling of Active Aeroservoelastic Systems

Anthony Su

A thesis

submitted in partial fulfillment of the

requirements for the degree of

Master of Science in Aeronautics & Astronautics

University of Washington

2023

Committee:

Name of Chairperson

First committee member

Next committee member

etc

Program Authorized to Offer Degree:

William E. Boeing Department of Aeronautics & Astronautics

University of Washington

Abstract

Modeling of Active Aeroservoelastic Systems

Anthony Su

Chair of the Supervisory Committee:
Title of Chair Name of Chairperson
William E. Boeing Department of Aeronautics & Astronautics

Lorem ipsum dolor sit amet, consectetur adipiscing elit. Nunc et maximus tortor, eget congue lectus. Suspendisse quis sodales mi. In faucibus libero vel condimentum ornare. Suspendisse a erat porta justo suscipit porttitor at et magna. Duis vitae egestas eros. Curabitur enim ex, tempus et nunc eget, interdum convallis nisi. In hac habitasse platea dictumst. Curabitur a nisl non turpis fermentum tincidunt. Vestibulum ante ipsum primis in faucibus orci luctus et ultrices posuere cubilia curae; Curabitur euismod molestie nulla, non molestie sem hendrerit vel. Pellentesque dapibus vulputate urna et dignissim. Morbi condimentum, velit quis fermentum faucibus, velit tellus scelerisque enim, a feugiat quam nulla in enim. Duis sed neque eget lorem condimentum varius vitae quis magna. Cras viverra posuere lorem, in fermentum leo porta a. Nam accumsan neque ut pretium volutpat.

TABLE OF CONTENTS

LIST OF FIGURES

LIST OF TABLES

NOMENCLATURE

Notation

[ ]	=	matrix
{ }	=	column vector

Abbreviations

CZT	=	chirp Z-transform
DFT	=	discrete Fourier transform
FEA	=	finite element analysis
FRF	=	frequency response function
GLA	=	gust load alleviation
GVT	=	ground vibration testing
HIL	=	hardware-in-the-loop
LE	=	leading edge
MARGE	=	Model for Aeroelastic Response to Gust Excitation
ODE	=	ordinary differential equation
SISO	=	single-input single-output
TE	=	trailing edge

Variables

b	=	reference semi-chord
j	=	imaginary unit
k	=	reduced frequency
N_s	=	# of elastic modes available
n_s	=	# of elastic modes used in modeling

n_c	=	# of rigid-body modes used in modeling
n_{lag}	=	# of lag terms used in modeling
q_D	=	dynamic pressure
s	=	Laplace variable
U	=	airspeed

Subscripts

s	=	structural (flexible) component
c	=	control (rigid) component
p	=	plant
act	=	actuator
sens	=	sensor

ACKNOWLEDGMENTS

I must first and foremost thank Professor Eli Livne for his mentorship and support throughout my foray into aeroelasticity and control. His passion for aeroelasticity and aeronautics has proven to be contagious and for that I am grateful. I would like to thank colleagues John Berg and Eddie Ting for their patience and readiness to lend their experience. Thanks also to Professor Marat Mor for his invaluable expertise and assistance in finite-element modeling; this work would not have been possible without him. Finally, I would like to thank all of the colleagues, friends, and family who have walked alongside me throughout this journey.

DEDICATION

to Lorem Ipsum, my dear friend

Chapter 1

INTRODUCTION

talk about aeronautics

talk about aerodynamics

talk about structural dynamics

talk about aeroelasticity

talk about control

talk about aeroservoelasticity

talk about MARGE

The goal of this project was to obtain a state-space model of MARGE in order to demonstrate low-cost active aeroservoelastic control.

The remainder of this document is organized as follows: Lorem Ipsum.

Chapter 2

SYSTEM DESCRIPTION

The subject of this study's modeling effort is the Model for Aeroelastic Response to Gust Excitation (MARGE). MARGE is a flexible half-span wing-body-tail wind tunnel model which is capable of rigid-body rotation in the pitch axis. It was designed to allow rapid and accessible testing of gust alleviation control laws. Thus, it is of a simple and affordable construction. Details of the original design and construction of MARGE can be found in [3].

The structure of MARGE consists of flexible beams encapsulated by lightweight aerodynamic shells. The wing and tail spars are made of aluminum while the fuselage is made of steel. The aerodynamic shells are made of polylactic acid (PLA) and form a symmetrical NACA 0012 airfoil. There is a brass mass fixed at the wing tip to bring the structure's natural frequencies to the designed magnitude. The wing is joined to the fuselage at its root and the entire assembly rotates about a shaft which is suspended from the hanging sub-assembly by bearings. A diagram of the structural configuration of MARGE is shown in Fig. 2.1.

MARGE has three actuators: two servo-actuated control surfaces on the wing and one servo-actuated elevator on the tail. There are also two servo-activated gust vanes installed upstream of the test section in the 3x3 low-speed wind tunnel. The gust vanes move in unison to generate discrete or continuous gusts and are controlled as a single actuator.

MARGE has five sensors. There are two unidirectional accelerometers at the wingtip, one ahead of the wing spar and one aft of the wing spar. There is another unidirectional accelerometer at the tip of the tail. (All three accelerometers are aligned normal to the lifting surfaces.) There is a strain gauge at the wing root. Finally, there is a hall effect sensor inside the hanging sub-assembly by the model's rotating shaft. There is a magnet fixed to the shaft which allows the hall effect sensor to measure the rotation of the shaft. A diagram of the
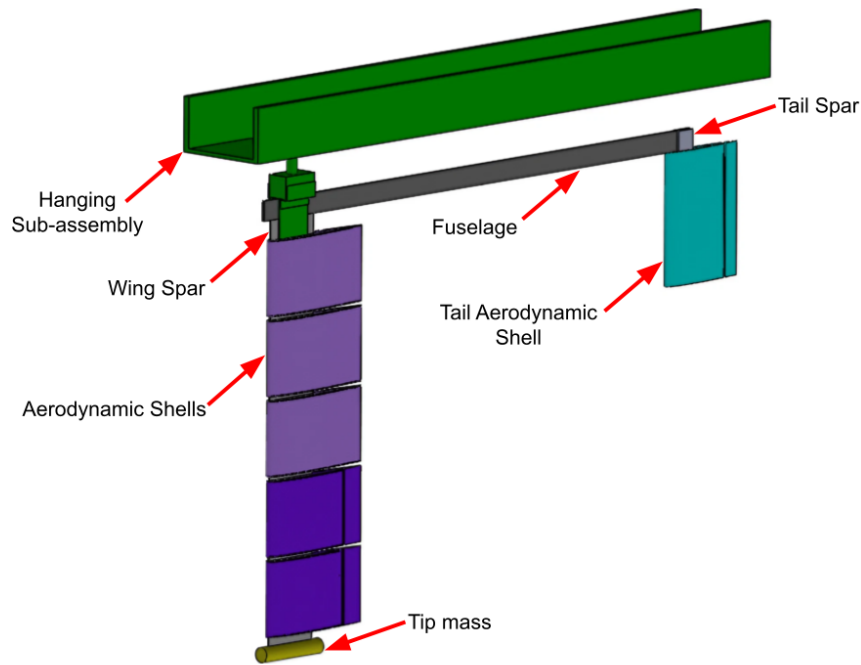
Figure 2.1: MARGE structural configuration

sensing and actuation configuration of MARGE is shown in Fig. 2.2.

Note that the sensor configuration is modified from the original design specified in [3]. The original design featured potentiometers on the control surfaces and a strain gauge on the fuselage. It also lacked the accelerometer on the tail. The potentiometers and the fuselage strain gauge have since been removed because they were found to be unnecessary. The accelerometer on the tail has since been added with the intent of capturing fuselage and tail flexible motions.

MARGE is designed to fit into the University of Washington's 3x3 low-speed wind tunnel. The 3x3 low-speed wind tunnel is an open-loop wind tunnel capable of speeds up to 60 m/s. The wind tunnel has flow straighteners, a 9:1 contraction, gust vanes, and a 3 ft. by 3 ft. by 8 ft. test section. Further details about the 3x3 low-speed wind tunnel can be found in [2]. When installed, MARGE hangs vertically from the ceiling of the test section. A diagram
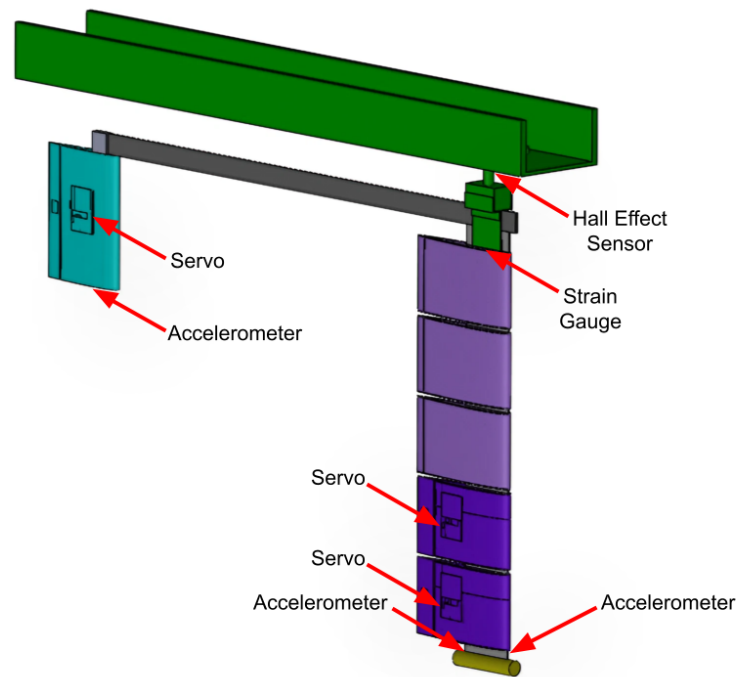
Figure 2.2: MARGE sensing and actuation configuration

indicating the key features of the 3x3 low-speed wind tunnel is shown in Fig. 2.3.

The physical interface to MARGE's acutation and sensing is a National Instruments DAQ coupled with a National Instruments terminal block. The exceptions to this are the gust vanes, which are controlled through HTTP on the local network. Data is transmitted and received to and from these interfaces through Simulink Real-Time.
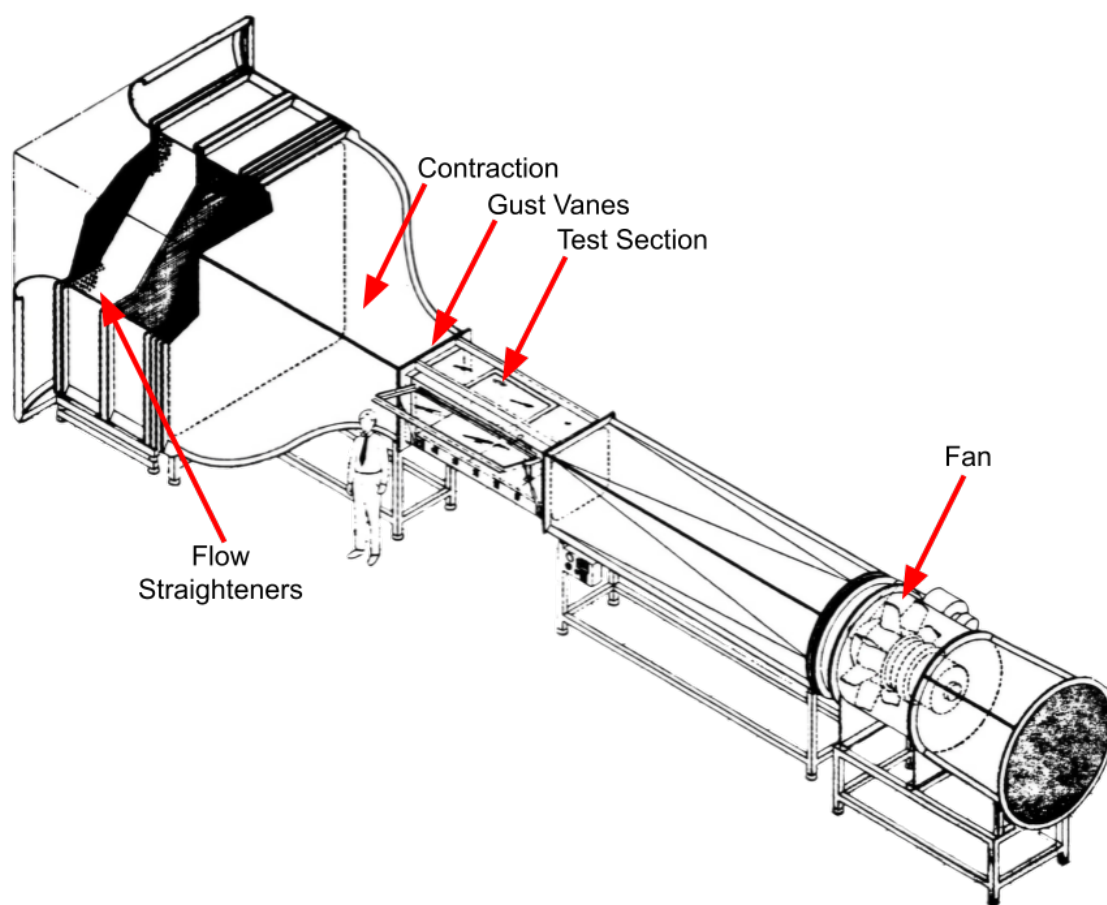
Figure 2.3: Univeristy of Washington 3x3 low-speed wind tunnel

<div align="center">

Chapter 3

DYNAMIC SYSTEM MODELING

</div>

The goal of this section is to derive a preliminary state-space model for the MARGE in the form

$$s\{x\} = [A]\{x\} + [B]\{u\}$$
$$\{y\} = [C]\{x\} + [D]\{u\}$$

(3.1)

based on first principles.

3.1 Plant Dynamics

This section will derive the plant dynamics for MARGE in the form

$$s\{x\} = [A_p]\{x_p\} + [B_p]\{u_p\}$$

(3.2)

3.1.1 Structural Dynamics

MARGE's structure is modeled as a linear, second-order system with damping and external forcing. The equations of motion for such a system are

$$s^2[M]\{q(s)\} + s[C]\{q(s)\} + [K]\{q(s)\} = \{f(s)\}$$

(3.3)

where $\{q\}$ is the structural dynamic state expressed in generalized modal coordinates, $\{f(s)\}$ is the generalized external forcing, and $[M]$, $[C]$, and $[K]$ are generalized mass, damping, and stiffness matrices respectively. Note that the modal coordinates include both elastic motions (of the structure) denoted by the subscript s and rigid-body motions (of the structure and the control surfaces) denoted by the subscript c:

$$\{q\} = \begin{Bmatrix} q_s \\ q_c \end{Bmatrix}$$

(3.4)

The forcing for the aeroservoelastic wing can be decomposed into the aerodynamic forcing due to the state and the forcing from actuator hinge moments:

$$s^2[M]\{q(s)\} + s[C]\{q(s)\} + [K]\{q(s)\} = q_D[A(s)]\{q(s)\} + \begin{Bmatrix} \{0\} \\ \{H_c\} \end{Bmatrix} \qquad (3.5)$$

where $[A(s)]$ is the aerodynamic influence matrix for the state and $\{H_c\}$ are the hinge moments from the actuators.

The whole system can be further decomposed into structural and control components:

$$\left(s^2 \begin{bmatrix} [M_{ss}] & [M_{sc}] \\ [M_{cs}] & [M_{cc}] \end{bmatrix} + s \begin{bmatrix} [C_{ss}] & [C_{sc}] \\ [C_{cs}] & [C_{cc}] \end{bmatrix} + \begin{bmatrix} [K_{ss}] & [K_{sc}] \\ [K_{cs}] & [K_{cc}] \end{bmatrix} \right) \begin{Bmatrix} \{q_s(s)\} \\ \{q_c(s)\} \end{Bmatrix}$$
$$= q_D \begin{bmatrix} [A_{ss}(s)] & [A_{sc}(s)] \\ [A_{cs}(s)] & [A_{cc}(s)] \end{bmatrix} \begin{Bmatrix} \{q_s(s)\} \\ \{q_c(s)\} \end{Bmatrix} + \begin{Bmatrix} \{0\} \\ \{H_c\} \end{Bmatrix} \qquad (3.6)$$

The control modes are those corresponding to rigid-body motions of control surfaces. The structural modes are all other modes, including flexible-body modes and rigid-body pitching of the entire model.

It is assumed that the dynamics of the control modes are completely determined by the control inputs and the inputs are not directly affected by the control modes, i.e. the actuators are irreversible controls. Then, interest is only in the dynamics of the structural modes:

$$\left(s^2 \begin{bmatrix} [M_{ss}] & [M_{sc}] \end{bmatrix} + s \begin{bmatrix} [C_{ss}] & [C_{sc}] \end{bmatrix} + \begin{bmatrix} [K_{ss}] & [K_{sc}] \end{bmatrix} \right) \begin{Bmatrix} \{q_s(s)\} \\ \{q_c(s)\} \end{Bmatrix}$$
$$= q_D \begin{bmatrix} [A_{ss}(s)] & [A_{sc}(s)] \end{bmatrix} \begin{Bmatrix} \{q_s(s)\} \\ \{q_c(s)\} \end{Bmatrix} \qquad (3.7)$$

Note that since the control modes are rigid-body modes, they have no stiffness and the

equations of motion further simplify to

$$\left(s^2 \begin{bmatrix} [M_{ss}] & [M_{sc}] \end{bmatrix} + s \begin{bmatrix} [C_{ss}] & [C_{sc}] \end{bmatrix} + \begin{bmatrix} [K_{ss}] & [0] \end{bmatrix} \right) \begin{Bmatrix} \{q_s(s)\} \\ \{q_c(s)\} \end{Bmatrix}$$

$$= q_D \begin{bmatrix} [A_{ss}(s)] & [A_{sc}(s)] \end{bmatrix} \begin{Bmatrix} \{q_s(s)\} \\ \{q_c(s)\} \end{Bmatrix} \quad (3.8)$$

3.1.2 The Roger Approximation

The aerodynamic influence matrix $[A]$ is a function of the Laplace variable s. For a thin airfoil oscillating in a potential flow, Theodorsen's solution applies [6]. This solution is nonlinear and unable to be represented in a linear system. In order to obtain the linear state-space system, $[A]$ must be approximated as an analytic function of s.

The Roger approximation [4] is a method of generating a rational function approximation of the aerodynamic influence matrix in the form

$$[A(s)] \approx [P_0] + s[P_1] + s^2[P_2] + \sum_{n=1}^{N_{\text{lag}}} \frac{s}{s + \beta_n} [P_{n+2}] \quad (3.9)$$

where $[P]$ are the unknown real-valued matrices that are fit to tabulated known $[A(s)]$ matrices (obtained from an unsteady aerodynamic solver such as that found in NASTRAN). Aside from the zeroth, first, and second order terms, there are N_{lag} additional "lag term" approximating functions which are defined by their respective constants β.

Begin with an approximation only along the frequency domain:

$$[A(jk)] \approx [\bar{P}_0] + jk[\bar{P}_1] + (jk)^2[\bar{P}_2] + \sum_{n=1}^{N_{\text{lag}}} \frac{jk}{jk + \bar{\beta}_n} [\bar{P}_{n+2}] \quad (3.10)$$

where k is the reduced frequency

$$k = \frac{\omega \cdot b}{U} \quad (3.11)$$

Given the tabulated set of aerodynamic influence matrices $[A]$ computed across N reduced frequencies, each entry p of the matrices $[\bar{P}]$ in the above approximation can be fit to the

corresponding entries a of the aerodynamic influence matrices $[A]$. The steady-state component of the approximation $[\bar{P}_0]$ is fixed to be equal to the steady-state aerodynamic influence matrix (with zero reduced frequency):

$$[\bar{P}_0] = [A(k = 0)] \tag{3.12}$$

The remaining $[\bar{P}]$ matrices are determined using a linear regression:

$$
\begin{bmatrix}
0 & -k_1^2 & \frac{k_1^2}{k_1^2+\bar{\beta}_1^2} & \cdots & \frac{k_1^2}{k_1^2+\bar{\beta}_{N_{\text{lag}}}^2} \\
k_1 & 0 & \frac{k_1\bar{\beta}_1}{k_1^2+\bar{\beta}_1^2} & \cdots & \frac{k_1\bar{\beta}_1}{k_1^2+\bar{\beta}_{N_{\text{lag}}}^2} \\
\vdots & \vdots & \vdots & & \vdots \\
0 & -k_N^2 & \frac{k_N^2}{k_N^2+\bar{\beta}_1^2} & \cdots & \frac{k_N^2}{k_N^2+\bar{\beta}_{N_{\text{lag}}}^2} \\
k_N & 0 & \frac{k_N\bar{\beta}_1}{k_N^2+\bar{\beta}_1^2} & \cdots & \frac{k_N\bar{\beta}_1}{N^2+\bar{\beta}_{N_{\text{lag}}}^2}
\end{bmatrix}
\left\{
\begin{array}{c}
\bar{p}_1 \\
\vdots \\
\bar{p}_{N_{\text{lag}}+2}
\end{array}
\right\}
=
\left\{
\begin{array}{c}
\text{Re}(a(jk_1)) - a(0) \\
\text{Im}(a(jk_1)) \\
\vdots \\
\text{Re}(a(jk_N)) - a(0) \\
\text{Im}(a(jk_N))
\end{array}
\right\}
\tag{3.13}
$$

The linear regression in Eq. 3.13 can then be solved using the method of least-squares to obtain the fitted $[\bar{P}]$ matrices.

Replacing the reduced frequency with the equivalent angular frequency yields

$$[A(j\omega)] \approx [P_0] + j\omega[P_1] - \omega^2[P_2] + \sum_{n=1}^{N_{\text{lag}}} \frac{j\omega}{j\omega + \beta_n}[P_{n+2}] \tag{3.14}$$

where

$$[P_0] = [\bar{P}_0]$$

$$[P_1] = [\bar{P}_1]\frac{b}{U}$$

$$[P_2] = [\bar{P}_2]\left(\frac{b}{U}\right)^2$$

$$[P_3] = [\bar{P}_3]$$

$$\vdots \tag{3.15}$$

$$[P_{N_{\text{lag}}+2}] = [\bar{P}_{N_{\text{lag}}+2}]$$

$$\beta_1 = \bar{\beta}_1\frac{U}{b}$$

$$\vdots$$

$$\beta_{N_{\text{lag}}} = \bar{\beta}_{N_{\text{lag}}}\frac{U}{b}$$

This is then extended from the imaginary axis to the full Laplace domain through analytic continuation, leading to the final form of the Roger approximation for aerodynamic influence matrices:

$$[A(s)] \approx [P_0] + s[P_1] + s^2[P_2] + \sum_{n=1}^{N_{\text{lag}}} \frac{s}{s + \beta_n}[P_{n+2}] \tag{3.16}$$

It should be noted that the Roger approximation is only valid over the tabulated reduced frequency range. Thus, any result from the model is only valid if the airspeed that the model ia analyzed at is sufficiently above

$$U_{\text{min}} = \frac{\omega_{\text{max}} \cdot b}{k_{\text{max}}} \tag{3.17}$$

where ω_{max} is the maximum frequency of interest in the analysis. Thus, modeling which utilizes the Roger Approximation cannot be used for purely structural dynamic analysis (where $U = 0$).

3.1.3   Coupled Aeroelastic Dynamics

This section describes how the structural dynamic equations of motion can be reduced to the form in Eq. 3.2.

Replacing the aerodynamic influence matrices in Eq. 3.8 with the equivalent Roger approximation and collecting like terms yields

$$\left(s^2[M_{ss}] + s[C_{ss}] + [K_{ss}] - q_D \left([P_{ss,0}] + s[P_{ss,1}] + s^2[P_{,2}] + \sum_{n=1}^{N_{\text{lag}}} \frac{s}{s + \beta_n}[P_{ss,n+2}] \right) \right) \{q_s(s)\}$$

$$= - \left(s^2[M_{sc}] + s[C_{sc}] - q_D \left([P_{sc,0}] + s[P_{sc,1}] + s^2[P_{sc,2}] + \sum_{n=1}^{N_{\text{lag}}} \frac{s}{s + \beta_n}[P_{sc,n+2}] \right) \right) \{q_c(s)\}$$

$$\tag{3.18}$$

Define the following coupled aeroelastic mass, damping, and stiffness matrices:

$$
\begin{aligned}
\left[\bar{\bar{M}}\right] &= [M] - q_D[P_2] \\
\left[\bar{\bar{C}}\right] &= [C] - q_D[P_1] \\
\left[\bar{\bar{K}}\right] &= [K] - q_D[P_0]
\end{aligned}
\tag{3.19}
$$

Equation 3.18 then simplifies to

$$
\left(s^2\left[\bar{\bar{M}}_{ss}\right] + s\left[\bar{\bar{C}}_{ss}\right] + \left[\bar{\bar{K}}_{ss}\right]\right)\{q_s(s)\} - q_D\left(\sum_{n=1}^{N_{\text{lag}}} \frac{s}{s+\beta_n}[P_{ss,n+2}]\right)\{q_s(s)\}
$$

$$
= -\left(s^2\left[\bar{\bar{M}}_{sc}\right] + s\left[\bar{\bar{C}}_{sc}\right] + \left[\bar{\bar{K}}_{sc}\right]\right)\{q_c(s)\} + q_D\left(\sum_{n=1}^{N_{\text{lag}}} \frac{s}{s+\beta_n}[P_{sc,n+2}]\right)\{q_c(s)\} \tag{3.20}
$$

Rearranging the lag terms,

$$
\left(s^2\left[\bar{\bar{M}}_{ss}\right] + s\left[\bar{\bar{C}}_{ss}\right] + \left[\bar{\bar{K}}_{ss}\right]\right)\{q_s(s)\}
$$

$$
- q_D\left[\sum_{n=1}^{N_{\text{lag}}} \frac{s}{s+\beta_n}[P_{ss,n+2}] \quad \sum_{n=1}^{N_{\text{lag}}} \frac{s}{s+\beta_n}[P_{sc,n+2}] \quad\right]\begin{Bmatrix} q_s(s) \\ q_c(s) \end{Bmatrix}
$$

$$
= -\left(s^2\left[\bar{\bar{M}}_{sc}\right] + s\left[\bar{\bar{C}}_{sc}\right] + \left[\bar{\bar{K}}_{sc}\right]\right)\{q_c(s)\} \tag{3.21}
$$

Define the following aerodynamic "lag states" as

$$
\{r_1\} = \left[[P_{ss,3}] \quad [P_{sc,3}]\right]\frac{s}{s+\beta_1}
$$

$$
\vdots \tag{3.22}
$$

$$
\{r_{N_{\text{lag}}}\} = \left[[P_{ss,N_{\text{lag}}+2}] \quad [P_{sc,N_{\text{lag}}+2}]\right]\frac{s}{s+\beta_{N_{\text{lag}}}}
$$

Rearranging this yields an expression for the first derivative of the lag states:

$$
s\{r_1\} = s[P_{ss,3}]\{q_s(s)\} + s[P_{sc,3}]\{q_c(s)\} - \beta_1\{r_1\}
$$

$$
\vdots \tag{3.23}
$$

$$
s\{r_{N_{\text{lag}}}\} = s[P_{ss,N_{\text{lag}}+2}]\{q_s\} + s[P_{sc,N_{\text{lag}}+2}]\{q_c\} - \beta_{N_{\text{lag}}}\{r_{N_{\text{lag}}}\}
$$

Combining these lag state dynamic equations into a single matrix equation yields

$$s\{r\} = s[B_{rs}]\{q_s\} + s[B_{rc}]\{q_c\} + [A_r]\{r\} \tag{3.24}$$

where $\{r\}$, $[B_{rs}]$, $[B_{rc}]$, and $[A_r]$ are defined as

$$\{r\} = \begin{Bmatrix} \{r_1\} \\ \vdots \\ \{r_{N_{\text{lag}}}\} \end{Bmatrix}$$

$$[B_{rs}] = \begin{bmatrix} [P_{ss,3}] \\ \vdots \\ [P_{ss,N_{\text{lag}}+2}] \end{bmatrix}$$

$$[B_{rc}] = \begin{bmatrix} [P_{sc,3}] \\ \vdots \\ [P_{sc,N_{\text{lag}}+2}] \end{bmatrix} \tag{3.25}$$

$$[A_r] = \begin{bmatrix} -\beta_1[I] & & \\ & \ddots & \\ & & -\beta_{N_{\text{lag}}}[I] \end{bmatrix}$$

With the lag states defined, Eq.3.21 can now be rewritten as

$$\left(s^2 \left[\bar{\bar{M}}_{ss}\right] + s \left[\bar{\bar{C}}_{ss}\right] + \left[\bar{\bar{K}}_{ss}\right]\right) \{q_s(s)\} - q_D \sum_{n=1}^{N_{\text{lag}}} \{r_n\}$$
$$= -\left(s^2 \left[\bar{\bar{M}}_{sc}\right] + s \left[\bar{\bar{C}}_{sc}\right] + \left[\bar{\bar{K}}_{sc}\right]\right) \{q_c(s)\} \tag{3.26}$$

The sum of lag states can be simplifed introducing the matrix $[I_r]$ such that

$$\{r_1\} + \cdots + \{r_{N_{\text{lag}}}\} = \begin{bmatrix} [I] & \cdots & [I] \end{bmatrix} \begin{Bmatrix} \{r_1\} \\ \vdots \\ \{r_{N_{\text{lag}}}\} \end{Bmatrix} = [I_r]\{r\} \tag{3.27}$$

This further compacts Eq. 3.26, which becomes

$$\left(s^2 \left[\bar{\bar{M}}_{ss} \right] + s \left[\bar{\bar{C}}_{ss} \right] + \left[\bar{\bar{K}}_{ss} \right] \right) \{q_s(s)\} - q_D[I_r]\{r\}$$
$$= - \left(s^2 \left[\bar{\bar{M}}_{sc} \right] + s \left[\bar{\bar{C}}_{sc} \right] + \left[\bar{\bar{K}}_{sc} \right] \right) \{q_c(s)\} \quad (3.28)$$

Define new structural dynamic state vectors as

$$\{x_1\} = \{q\} \quad (3.29)$$

$$\{x_2\} = s\{q\} \quad (3.30)$$

Using these, Eq. 3.28 can be rewritten as a first-order linear ODE for $\{x_2\}$:

$$s\{x_2\} = - \left[\bar{\bar{M}}_{ss} \right]^{-1} \left[\bar{\bar{C}}_{ss} \right] \{x_2\} - \left[\bar{\bar{M}}_{ss} \right]^{-1} \left[\bar{\bar{K}}_{ss} \right] \{x_1\} + q_D \left[\bar{\bar{M}}_{ss} \right]^{-1} [I_r]\{r\}$$
$$- \left[\bar{\bar{M}}_{ss} \right]^{-1} \left(s^2 \left[\bar{\bar{M}}_{sc} \right] + s \left[\bar{\bar{C}}_{sc} \right] + \left[\bar{\bar{K}}_{sc} \right] \right) \{q_c(s)\} \quad (3.31)$$

Rearranging,

$$s\{x_2\} = - \left[\bar{\bar{M}}_{ss} \right]^{-1} \left[\bar{\bar{C}}_{ss} \right] \{x_2\} - \left[\bar{\bar{M}}_{ss} \right]^{-1} \left[\bar{\bar{K}}_{ss} \right] \{x_1\}$$
$$+ q_D \left[\bar{\bar{M}}_{ss} \right]^{-1} [I_r]\{r\} - \left[\bar{\bar{M}}_{ss} \right]^{-1} \left[\left[\bar{\bar{K}}_{sc} \right] \quad \left[\bar{\bar{C}}_{sc} \right] \quad \left[\bar{\bar{M}}_{sc} \right] \right] \left\{ \begin{array}{c} \{q_c(s)\} \\ s\{q_c(s)\} \\ s^2\{q_c(s)\} \end{array} \right\} \quad (3.32)$$

Define the following simplifying matrices:

$$[T_{21}] = - \left[\bar{\bar{M}}_{ss} \right]^{-1} \left[\bar{\bar{K}}_{ss} \right] \quad (3.33)$$

$$[T_{22}] = - \left[\bar{\bar{M}}_{ss} \right]^{-1} \left[\bar{\bar{C}}_{ss} \right] \quad (3.34)$$

$$[T_{2r}] = q_D \left[\bar{\bar{M}}_{ss} \right]^{-1} [I_r] \quad (3.35)$$

$$[T_{2c}] = - \left[\bar{\bar{M}}_{ss} \right]^{-1} \left[\left[\bar{\bar{K}}_{sc} \right] \quad \left[\bar{\bar{C}}_{sc} \right] \quad \left[\bar{\bar{M}}_{sc} \right] \right] \quad (3.36)$$

Equation 3.32 then simplifies to

$$s\{x_2\} = [T_{21}]\{x_1\} + [T_{22}]\{x_2\} + [T_{2r}]\{r\} + [T_{2c}]\{q_c\} \quad (3.37)$$

Now there exist first-order linear ODEs for the structural dynamic states (Eq. 3.32) and the aerodynamic lag states (Eq. 3.24) so the dynamics of the full system can be written in state-space form:

$$s \begin{Bmatrix} \{x_1\} \\ \{x_2\} \\ \{r\} \end{Bmatrix} = \begin{bmatrix} [0] & [I] & [0] \\ [T_{21}] & [T_{22}] & [T_{2r}] \\ [0] & [B_{rs}] & [A_r] \end{bmatrix} \begin{Bmatrix} \{x_1\} \\ \{x_2\} \\ \{r\} \end{Bmatrix} + \begin{bmatrix} [0] & [0] & [0] \\ [& T_{2c} &] \\ [0] & [B_{rc}] & [0] \end{bmatrix} \begin{Bmatrix} \{q_c\} \\ s\{q_c\} \\ s^2\{q_c\} \end{Bmatrix} \qquad (3.38)$$

Define the state vector of the MARGE plant to be

$$\{x_p\} = \begin{Bmatrix} \{x_1\} \\ \{x_2\} \\ \{r\} \end{Bmatrix} \qquad (3.39)$$

and the input vector of the MARGE plant to be

$$\{u_p\} = \begin{Bmatrix} \{q_c\} \\ s\{q_c\} \\ s^2\{q_c\} \end{Bmatrix} \qquad (3.40)$$

Then, Eq. 3.38 can be written in the form that is desired:

$$s\{x_p\} = [A_p]\{x_p\} + [B_p]\{u_p\} \qquad (3.41)$$

where $[A_p]$ and $[B_p]$ are the block matrices in Eq. 3.38.

3.2 Plant Output Modeling

This section will derive the output equations for MARGE in the form

$$\{y_p\} = [C_p]\{x_p\} + [D_p]\{u_p\} \qquad (3.42)$$

The output of MARGE consists of three acceleration, one strain, and one pitch measurements. The plant output model to be presented here captures all of these as well as an

optional pitch rate output. Thus,

$$\{u_p\} = \begin{Bmatrix} \text{acceleration 1} \\ \text{acceleration 2} \\ \text{acceleration 3} \\ \text{strain} \\ \text{rotation} \\ \text{rotation rate} \end{Bmatrix} \tag{3.43}$$

These outputs are the inputs to the sensors described in the next section.

The structural dynamic generalized state $\{q\}$ has modal coordinates which correspond to n_s mode shapes of the structure $\{\phi_1\}, \ldots, \{\phi_{n_s}\}$. These modes shapes are in physical coordinates and are known from the structural dynamic solution of the finite-element model. The motion of the system in physical coordinates $\{z(t)\}$ is

$$\{z(t)\} = \begin{bmatrix} \{\phi_1\} & \cdots & \{\phi_{n_s}\} \end{bmatrix} \{q\} \tag{3.44}$$

For the ith degree of freedom (DOF) of the system, this is

$$z_i(t) = \begin{bmatrix} \phi^i \end{bmatrix} \{q(t)\} \tag{3.45}$$

where $[\phi^i]$ contains the contribution to that DOF's motion from each mode:

$$\begin{bmatrix} \phi^i \end{bmatrix} = \begin{bmatrix} \phi_1^i & \cdots & \phi_{n_s}^i \end{bmatrix} \tag{3.46}$$

The motion of the system can be expressed in terms of the full plant state vector defined in Eq. 3.39 as

$$\{z_i(t)\} = \begin{bmatrix} \phi^i \end{bmatrix} [T_{\text{disp}}]\{x_p(t)\} \tag{3.47}$$

where $[T_{\text{disp}}]$ is a matrix which extracts the $\{x_1\}$ component of $\{x_p\}$:

$$[T_{\text{disp}}] = \begin{bmatrix} [I]_{n_s \times n_s} & [0]_{n_s \times n_s} & [0]_{n_s \times n_{\text{lag}}} \end{bmatrix} \tag{3.48}$$

Here, n_s is the number of elastic "structural" modes used, n_c is the number of rigid-body "control" modes used, and n_{lag} is the number of lag terms used in the model.

Similarly, the rates of the system's motion at DOF i can be expressed using the $\{x_2\}$ component of the state vector $\{x_p\}$:

$$\frac{\mathrm{d}\{z_i(t)\}}{\mathrm{d}t} = \left[\phi^i\right] [T_{\text{vel}}]\{x_p(t)\} \tag{3.49}$$

where $[T_{\text{vel}}]$ is a matrix which extracts the $\{x_2\}$ component of $\{x_p\}$:

$$[T_{\text{vel}}] = \left[[0]_{n_s \times n_s} \quad [I]_{n_s \times n_s} \quad [0]_{n_s \times n_{\text{lag}}} \right] \tag{3.50}$$

3.2.1 Acceleration Output

The system's accelerations at DOF i can then be expressed as

$$\frac{\mathrm{d}^2\{z_i(t)\}}{\mathrm{d}t^2} = \left[\phi^i\right] [T_{\text{vel}}] \frac{\mathrm{d}\{x_p(t)\}}{\mathrm{d}t} \tag{3.51}$$

The derivative of $\{x_p(t)\}$ is contained in Eq. 3.38. Using that expression here yields

$$\frac{\mathrm{d}^2\{z_i(t)\}}{\mathrm{d}t^2} = \left[\phi^i\right] [T_{\text{vel}}] \left([A_p]\{x_p\} + [B_p]\{u_p(t)\}\right) \tag{3.52}$$

For the three accelerometer locations (DOFs) on MARGE with corresponding modal motions $\{\phi_1\}$, $\{\phi_2\}$, and $\{\phi_3\}$, the accelerations experienced by the sensors are

$$\begin{Bmatrix} y_1(t) \\ y_2(t) \\ y_3(t) \end{Bmatrix} = \begin{bmatrix} \left[\phi^1\right] [T_{\text{vel}}][A_p] \\ \left[\phi^2\right] [T_{\text{vel}}][A_p] \\ \left[\phi^3\right] [T_{\text{vel}}][A_p] \end{bmatrix} \{x_p(t)\} + \begin{bmatrix} \left[\phi^1\right] [T_{\text{vel}}][B_p] \\ \left[\phi^2\right] [T_{\text{vel}}][B_p] \\ \left[\phi^3\right] [T_{\text{vel}}][B_p] \end{bmatrix} \{u_p(t)\} \tag{3.53}$$

3.2.2 Pitch Output

For the pitch output which is a measure of position instead of acceleration, Eq. 3.47 is used instead:

$$u_5(t) = \left[\phi^5\right] [T_{\text{disp}}]\{x_p(t)\} \tag{3.54}$$

The corresponding pitch rate output is similarly given by 3.49

$$u_6(t) = \left[\phi^5\right] [T_{\text{vel}}]\{x_p(t)\} \tag{3.55}$$

Note that the pitch rate output uses the same DOF in the mode shape (ϕ^5) as the pitch output.

3.2.3 Strain Output

The structural dynamic generalized state $\{q\}$ has modal coordinates which also correspond to the load (force or moment) at each DOF in each of n_s mode shapes of the structure $\{\psi_1\}, \ldots, \{\psi_{n_s}\}$. (This is also known from the finite element model.) The loading state of the system in physical coordinates $\{L(t)\}$ is

$$\{L(t)\} = \left[\{\psi_1\} \quad \cdots \quad \{\psi_{n_s}\}\right]\{q(t)\} \tag{3.56}$$

For the ith DOF of the system,

$$L_i(t) = [\psi^i]\{q(t)\} \tag{3.57}$$

where

$$\psi^i = \left[\psi_1^i \quad \cdots \quad \psi_{n_s}^i\right]\{q(t)\} \tag{3.58}$$

In a similar fashion as in Eq. 3.47, this DOF's load can be expressed in terms of the system state:

$$\psi^i = \left[\psi_1^i \quad \cdots \quad \psi_{n_s}^i\right][T_{\text{disp}}]\{x_p(t)\} \tag{3.59}$$

Given this load, the strain due to bending is deteremined using the following relation from Euler-Bernoulli linear beam theory:

$$\varepsilon_y = -\frac{M_x \cdot z}{I_{zz} \cdot E} \tag{3.60}$$

where ε_y is the strain, M_x is the bending moment (from the relevant DOF of $\{L\}$), z is the z-distance of the sensor from the elastic axis of the beam, I_{zz} is the z-axis area moment of inertia, and E is the modulus of elasticity. Although the axial load in the y-direction would also add to the strain output, its effect is negligible compared to that of bending. This is especially true because the axial y-stress at rest due to the weight of the model is tared out at before tests. Thus, its effect has been ommitted in modeling.

The strain gauge on MARGE is mounted on the lower surface of the rectangular cross-sectioned wing spar. Thus, z is equal to negative one half of the spar thickness t:

$$\varepsilon_y = -\frac{M_x \cdot (-t/2)}{I_{zz} \cdot E} \tag{3.61}$$

Combining Eqs. 3.59 and yields the final expression for MARGE's strain output, u_4:

$$u_4 = \frac{t/2}{I_{zz} \cdot E} \begin{bmatrix} \psi_1^4 & \cdots & \psi_{n_s}^4 \end{bmatrix} [T_{\text{disp}}]\{x_p(t)\} \tag{3.62}$$

Thus, the full expression for the plant output of MARGE is

$$\{y_p\} = \begin{bmatrix} [\phi^1]\,[T_{\text{vel}}][A_p] \\ [\phi^2]\,[T_{\text{vel}}][A_p] \\ [\phi^3]\,[T_{\text{vel}}][A_p] \\ \frac{t/2}{I_{zz} \cdot E} \begin{bmatrix} \psi_1^4 & \cdots & \psi_{n_s}^4 \end{bmatrix} [T_{\text{disp}}] \\ [\phi^5]\,[T_{\text{disp}}] \\ [\phi^5]\,[T_{\text{vel}}] \end{bmatrix} \{x_p\} + \begin{bmatrix} [\phi^1]\,[T_{\text{vel}}][B_p] \\ [\phi^2]\,[T_{\text{vel}}][B_p] \\ [\phi^3]\,[T_{\text{vel}}][B_p] \\ 0 \\ 0 \\ 0 \end{bmatrix} \{u_p\} \tag{3.63}$$

Thus, the plant output of MARGE has been derived the form that is desired

$$\{y_p\} = [C_p]\{x_p\} + [D_p]\{u_p\} \tag{3.64}$$

where $[C_p]$ and $[D_p]$ are the block matrices in Eq. 3.63.

3.3 Actuation and Sensing Dynamics

When developing a model that is used for control design, the dynamics of the actuators and sensors must be accounted for. The output of the control law will be fed not into the

plant, but the imperfect actuators. The input of the control law will come not directly from the plant, but from the imperfect sensors. Thus, the goal of this section is to determine dynamic models for the actuators and the sensors in the forms

$$\frac{\mathrm{d}}{\mathrm{d}t}\{x_{\mathrm{act}}\} = [A_{\mathrm{act}}]\{x_{\mathrm{act}}\} + [B_{\mathrm{act}}]\{u_{\mathrm{act}}\}$$
$$\{y_{\mathrm{act}}\} = [C_{\mathrm{act}}]\{x_{\mathrm{act}}\} + [D_{\mathrm{act}}]\{u_{\mathrm{act}}\}$$

(3.65)

and

$$\frac{\mathrm{d}}{\mathrm{d}t}\{x_{\mathrm{sens}}\} = [A_{\mathrm{sens}}]\{x_{\mathrm{sens}}\} + [B_{\mathrm{sens}}]\{u_{\mathrm{sens}}\}$$
$$\{y_{\mathrm{sens}}\} = [C_{\mathrm{sens}}]\{x_{\mathrm{sens}}\} + [D_{\mathrm{sens}}]\{u_{\mathrm{sens}}\}$$

(3.66)

The servo-actuated control surfaces on the wing and tail are known (from [3]) to have dynamics according to the following transfer function[1]:

$$G(s) = \frac{1461}{s^2 + 62.2s + 1461}$$

(3.67)

This transfer function was then converted to the following equivalent state-space representation:

$$s\{x\} = \begin{bmatrix} -62.2 & -1461 \\ 1 & 0 \end{bmatrix} \{x\} + \begin{bmatrix} 0 \\ 1 \end{bmatrix} u$$
$$y = \begin{bmatrix} 0 & 1461 \end{bmatrix} \{x\}$$

(3.68)

where u is the input, y is the output, and $\{x\}$ is the internal state of the actuator.

The wind tunnel gust vanes were measured to have "perfect" dynamics except for a pure time delay of 0.34 seconds. This pure delay was approximated as a second-order transfer function using a Padé approximant:

$$G(s) = \frac{s^2 - 176.47s + 10381}{s^2 + 176.47s + 10381}$$

(3.69)

The Padé approximant matches the pure delay's response well in the frequency range of interest (<20 Hz); the step response and phase shift behavior of a pure delay and the Padé approximant are compared in Fig. 3.3.

---

[1]The numerator of this transfer function differs from that defined in [3] because the actuator is calibrated to have unity DC gain before use.
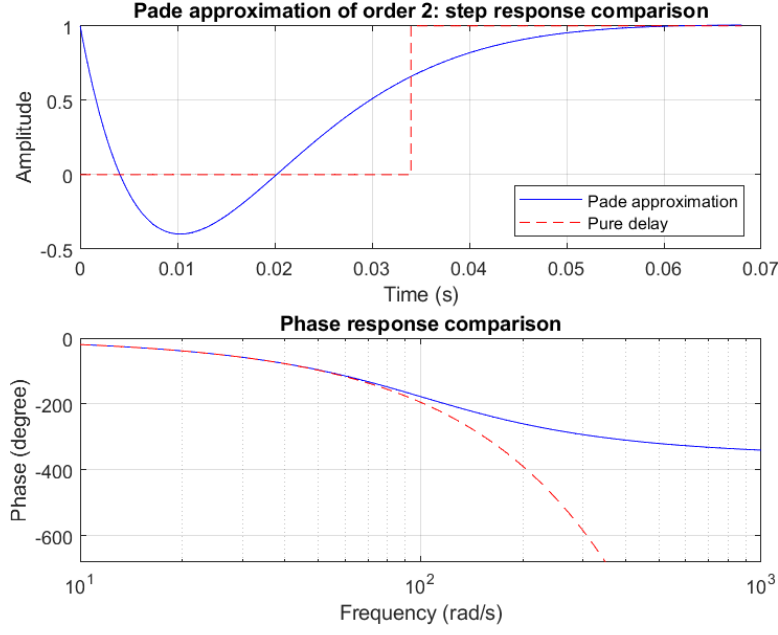
Figure 3.1: Padé approximant of the pure-delay response of the wind tunnel gust vanes

This transfer function was then converted to the following equivalent state-space representation:

$$
s\{x\} = \begin{bmatrix} -176.47 & -10381 \\ 1 & 0 \end{bmatrix} \{x\} + \begin{bmatrix} 1 \\ 0 \end{bmatrix} u
$$
$$
y = \begin{bmatrix} -352.94 & 0 \end{bmatrix} \{x\} + \begin{bmatrix} 1 \end{bmatrix} u
$$

(3.70)

where u is the input, y is the output, and $\{x\}$ is the internal state of the actuator.

The state-space models for the four actuators (three servo-actuated control surfaces and one pair of wind tunnel gust vanes) are combined to form one combined state-space model for all actuators with input, output, and state

$$
\{u_{\text{act}}\} = \begin{bmatrix} u_1 \\ u_2 \\ u_3 \\ u_4 \end{bmatrix} \qquad \{y_{\text{act}}\} = \begin{bmatrix} y_1 \\ y_2 \\ y_3 \\ y_4 \end{bmatrix} \qquad \{x_{\text{act}}\} = \begin{bmatrix} \{x\}_1 \\ \{x\}_2 \\ \{x\}_3 \\ \{x\}_4 \end{bmatrix}
$$

(3.71)

respectively. The combined actuation state-space model is then

$$
\{x_{\text{act}}\} = \begin{bmatrix} [A_1] & & & \\ & [A_2] & & \\ & & [A_3] & \\ & & & [A_4] \end{bmatrix} \{x_{\text{act}}\} + \begin{bmatrix} [B_1] & & & \\ & [B_2] & & \\ & & [B_3] & \\ & & & [B_4] \end{bmatrix} \{u_{\text{act}}\}
$$
$$
\{y_{\text{act}}\} = \begin{bmatrix} [C_1] & & & \\ & [C_2] & & \\ & & [C_3] & \\ & & & [C_4] \end{bmatrix} \{x_{\text{act}}\} + \begin{bmatrix} [D_1] & & & \\ & [D_2] & & \\ & & [D_3] & \\ & & & [D_4] \end{bmatrix} \{u_{\text{act}}\}
$$

(3.72)

where the $[A]$, $[B]$, $[C]$, and $[D]$ system matrices for the two types of actuators are defined above in Eq. 3.68 and 3.70. This then forms the actuator block shown in Fig. 3.4.

A similar process would be appropriate for a set of imperfect sensors. However, the high-rate sensors used in MARGE have approximately no dynamics in the frequency range of interest. Thus, the sensor response was approximated as

$$
\{y_{\text{sens}}\} = [I]\{u_{\text{sens}}\}
$$

(3.73)

In other words, the output of the sensor was taken as the output of the plant. This then forms the sensor block shown in Fig. 3.4.

3.4 *Coupled Aeroservoelastic Modeling*

The imperfect actuators and sensors can be accounted for in modeling by combining the actuator, plant, and sensor models into an integrated system model that can then be used for control design; see Fig. 3.4 for a block diagram of this system of systems. In the system illustration in Fig. 3.4, the actuators take in the control command and output control forces; the plant takes in control forces and outputs motions; the sensors take in motions and output measured motions; and a control law can then use this measured motion to create a control command for MARGE.
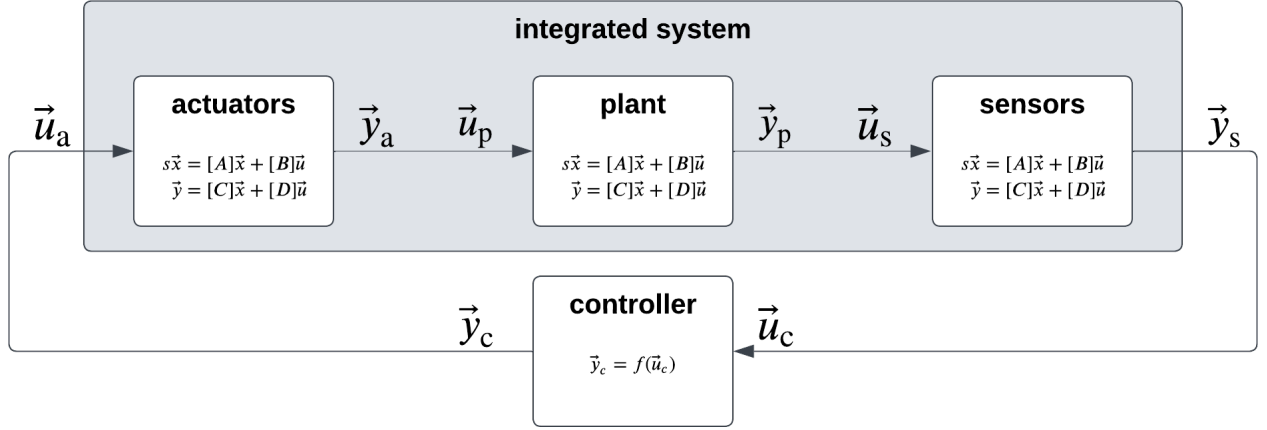
Figure 3.2: Integrated model of actuation, plant, and sensing in a control loop

First, the actuator dynamics can be coupled to the plant dynamics. In state-space form, this is

$$
s \left\{ \begin{array}{c} \{x_{\mathrm{act}}\} \\ \{x_p\} \end{array} \right\} = \left[\begin{array}{cc} [A_{\mathrm{act}}] & [0] \\ [B_p][C_{\mathrm{act}}] & [A_p] \end{array} \right] \left\{ \begin{array}{c} \{x_{\mathrm{act}}\} \\ \{x_p\} \end{array} \right\} + \left[\begin{array}{c} [B_{\mathrm{act}}] \\ [B_p][D_{\mathrm{act}}] \end{array} \right] \{u_{\mathrm{act}}\} \qquad (3.74)
$$

where the entries in the block matrices containing $[B_p]$ are used to convert $\{x_{\mathrm{act}}\}$ and $\{u_{\mathrm{act}}\}$ into the plant's input, $\{u_p\} = \{y_{\mathrm{act}}\}$.

The actuator can similarly be coupled to the plant in the output equations:

$$
\{y_p\} = \left[[D_p][C_{\mathrm{act}}] \quad [C_p] \right] \left\{ \begin{array}{c} \{x_{\mathrm{act}}\} \\ \{x_p\} \end{array} \right\} + [D_p][D_{\mathrm{act}}]\{u_{\mathrm{act}}\} \qquad (3.75)
$$

where similarly, the terms involving $[D_p]$ are used to convert $\{x_{\mathrm{act}}\}$ and $\{u_{\mathrm{act}}\}$ into the plant's input, $\{u_p\} = \{y_{\mathrm{act}}\}$.

The block matrices in Eq. 3.74 and 3.75 form the coupled actuator-plant system in Fig. 3.4. Since the sensors are modeled as perfect, this is also equivalent to the coupled actuator-plant-sensor system. Thus, Eq. 3.74 and 3.75 define the state-full, coupled space model for MARGE in the form required as defined in Eq. 3.1.

Chapter 4

FINITE ELEMENT MODELING

An aeroelastic finite element model of MARGE was previously constructed using NAS-TRAN. The model includes MARGE, the wind tunnel test section walls, and the gust vanes.

The wing structure and tail structure were each modeled as a single chain of Euler-Bernoulli beam elements along their respective spar. The wind tunnel walls were modeled as extremely stiff panels (which are approximately rigid).

The area moments of inertia of the beam elements in the finite element model are reported in Table 4.1.

Table 4.1: Area moment of inertia of beam finite elements

	I_1, m^4	I_2, m^4	J, m^4
wing spar	2.541×10^{-11}	5.853×10^{-8}	5.856×10^{-8}
tail spar	1.829×10^{-9}	1.301×10^{-8}	1.484×10^{-8}
fuselage	7.452×10^{-11}	4.476×10^{-9}	4.550×10^{-9}
rigid	2.541×10^{-11}	5.853×10^{-8}	5.856×10^{-8}

The aerodynamic loads on the NASTRAN model are based on the doublet-lattice model (DLM) of aerodynamics. This linear aerodynamic model assumes incompressible, inviscid, irrotational flow around thin lifting surfaces. The loads were transferred from the aerodynamic panels to the structural elements with NASTRAN

The loads on the finite element model were determined using doublet-lattice lifting surface theory which is <insert> The loads on the aerodynamic panels were transferred to the structural nodes via a spline interpolation.

The structural dynamic solution to the NASTRAN model yielded the natural modes which are described in the table below

Table 4.2: NASTRAN Modal Properties

#	ω_n	Description
1	0	pitching
2	1.444	wing bending 1
3	10.487	wing bending 2
4	16.638	fuselage bending 1
5	19.200	wing twisting 1
6	21.948	fuselage in-plane bending 1
7	32.311	wing bending 3
8	60.852	fuselage bending 2
9	66.011	wing bending 4
10	69.298	wing in-plane bending 1
11	113.674	wing bending 5
12	120.642	fuselage bending 3
13	153.716	fuselage in-plane bending 2
14	160.909	fuselage bending 4
15	175.941	wing bending 6

Chapter 5

GROUND VIBRATION TESTING

Ground vibration testing (GVT) was performed to validate the preliminary finite-element model of MARGE. The frequency responses of accelerometers to an impulse input were generated from the experimental data. Using these, the natural frequencies and the damping ratios of dynamic modes of the system were determined.

Two sets of data were collected. The first set of data was collected with MARGE as designed, including the rigid-body pitching mode. This data was used to determine the damping ratios of the modes. The second set of data was collected with the root of the MARGE wing clamped to eliminate the rotational rigid-body mode. This was done to enable data acquisition of flexible-body modes without exciting and losing energy to the rigid-body mode. This data was used to tune the finite-element model and to determine the damping ratios of the wing bending modes.

5.1   Test Setup

The equipment used for the test include:

- PCB Piezotronics ICP Impact Hammer Model 086C03

- PCB Piezotronics ICP Accelerometer Model 352C22

- National Instruments Breakout <insert>

- National Instruments DAQ Module <insert>

The impact hammer and accelerometers were connected to the DAQ system which was connected to a personal computer. The computer recorded data from the DAQ system using the Data Acquisition Toolbox for MATLAB.

5.1.1 Sensor Placement

The accelerometers were placed in locations such that all of the flexible natural modes of interest were observable. This was done by placing accelerometers near anti-nodal points of the natural modes as predicted by the preliminary finite-element model. The accelerometer locations for the two sets of testing are shown in Fig. 5.1. The impact hammer hits were also placed at these same locations on the structure as the accelerometers.
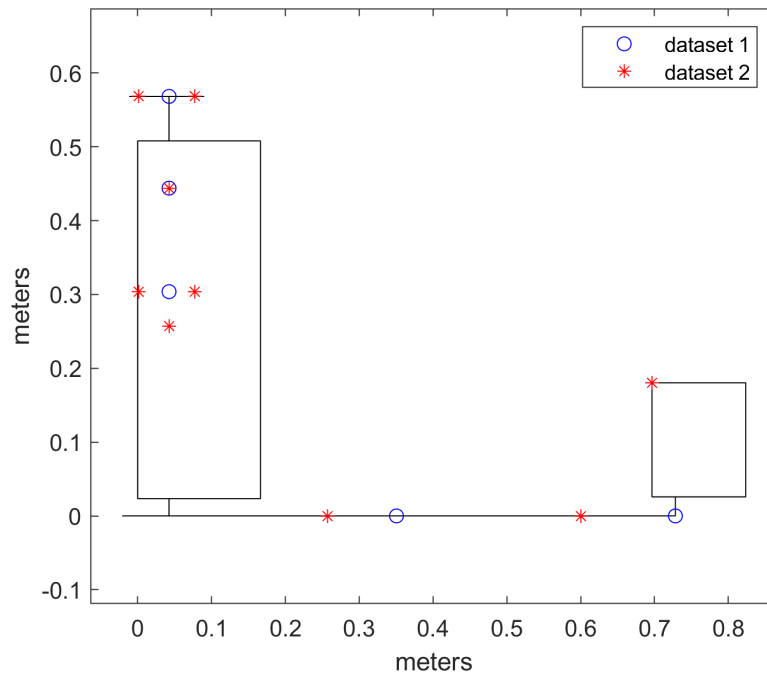

Figure 5.1: Accelerometer placement in ground vibration testing of MARGE

For the second dataset, pairs of accelerometers on the wing located a short distance apart chordwise were also treated as a fictional third accelerometer by taking the difference of their signals. This was done to simulate a sensor observing only torsional modes of the wing.

5.2   Generating Frequency Response Functions

Each GVT test point (input-output combination) was post-processed to generate the frequency response functions (FRFs) of the accelerometers to the impacts. This section describes the steps in this process.

5.2.1   Time-Domain Post-Processing

The time-series data was truncated to to start just before the impulse input and end after t seconds where t was chosen to be at least four times the period of the lowest frequency of interest. (In most cases, $t = 4$ seconds.) This ensured that irrelevant segments of the signal were eliminated while keeping still enough data to perform the frequency-domain analysis.

Each test point was recorded as three (in the second dataset) or five (in the first dataset) separate impacts. After truncation, the signals from these impacts were concatenated to form one continuous time-domain signal. The mean of this combined signal was then subtracted from it so that there would be no steady-state component before proceeding to compute the frequency response.

5.2.2   Computing Frequency Response Functions

The frequency response functions for each of these concatenated SISO signal pairs were computed using the method described in [7]. This section summarizes this method as it was implemented for the GVT data.

First, the signal was buffered into overlapping Hann windows and transformed using a chirp z-transform (CZT). The CZT is a generalization of the Discrete Fourier Transform (DFT) that can compute the Z-transform along an arc of the unit circle. Thus, it has an advantage over DFT in that it has the ability to allocate the full frequency-domain resolution to the bandwidth of interest. The purpose of first buffering the signal is to reduce the effect of noise at the expense of frequency resolution.

The products of the CZT are the power spectra of the signals. For any given accelerometer

power spectrum S_y and impact hammer power spectrum S_x, the frequency response function can then be computed as

$$FRF = \frac{G_{yy}}{G_{yx}} \tag{5.1}$$

where

$$G_{yx}(\omega) = S_y^* \cdot S_x \tag{5.2}$$

$$G_{yy}(\omega) = |S_y|^2 \tag{5.3}$$

The coherence can also be computed as

$$\text{coh}(\omega) = \frac{|G_{xy}|^2}{|G_{xx}||G_{yy}|} \tag{5.4}$$

where

$$G_{xy}(\omega) = S_x^* \cdot S_y \tag{5.5}$$

$$G_{yy}(\omega) = |S_y|^2 \tag{5.6}$$

The frequency response functions computed for the GVT data are shown in Appendix A.

5.3   Determining Modal Properties

Once the FRFs were computed, the frequencies and damping ratios of the natural modes were determined from the FRFs.

5.3.1   Computing Natural Frequencies

First, visible natural frequencies visible as peaks in the data were noted. These often were visible across multiple FRFs, confirming that they were not artifacts from the noise of a single experimental trial.

These experimental natural frequencies were compared to those predicted by the NAS-TRAN finite-element model; if they matched well, it was assumed that the experimental

natural frequency corresponded to the mode shape generated by the NASTRAN model. This could be further validated by observing the antinodal points of the relevant NASTRAN mode shape and checking that the FRFs in which the natural frequency peaks are visible correspond to sensors placed near those antinodal points.

In some cases, there were clear natural modes visible in the experimental data that were not predicted by the NASTRAN finite-element model. It was inferred that two of these natural modes appeared in that these were torsional modes of the wing, because the FRFs they appeared most prominently in were from the aforementioned "fictional" accelerometers which had manipulated signals to enhance the response to torsional modes. These torsional modes were not predicted by the preliminary NASTRAN finite-element model; this was corrected in the subsequent FEM tuning process.

Each experimental natural frequency ω_n was then measured in an automated way: first, all FRFs with a local maximum magnitude at ω_n which was at least twice the magnitude of its surroundings was identified. The median of all of these measured natural frequencies, each from a different FRF, was then taken to be the true experimental natural frequency for that nautral mode.

5.3.2   Computing Damping Ratios

The damping ratio was also measured in a similar automated way. The damping ratio was computed for each identifiable natural frequency in each FRF using the half-power method:

$$\zeta = \frac{\omega_2 - \omega_1}{2\omega_n} \tag{5.7}$$

where

$$\{\omega_1, \omega_2\} = \left\{ \omega \ \middle| \ FRF(\omega) = \frac{1}{2}FRF(\omega_n) \right\} \tag{5.8}$$

The median of all of these damping ratios, each from a different FRF was then taken to be the true damping ratio for that natural mode. The experimentally obtained natural frequencies and damping ratios can be found in Table 5.1.

Table 5.1: Experimental Natural Modes

ω_n	ζ	Description
0		pitching
1.422	0.030	wing bending 1
10.142	0.046	wing bending 2
18.094	0.113	wing twisting 1
19.893	0.033	fuselate in-plane bending 1
19.897	0.031	fuselage bending 1
32.545	0.019	wing bending 3
51.706	0.084	wing torsion 2
60.482	0.035	wing bending 4
74.521	0.023	fuselage bending 2

5.4 Finite Element Model Correction

The finite-element model was adjusted to better match the experimental GVT data. This was done by adjusting the bending and torsional stiffness of the various materials

Chapter 6

WIND TUNNEL TESTING AND MODEL TUNING

This chapter describes the wind-tunnel testing of MARGE and the tuning of the aeroservoelastic model to match the experimental data. It also discusses shortcomings of the data and lessons learned.

6.1   Data Acquisition and Analysis

MARGE's response was tested at the University of Washington's 3x3 low-speed wind tunnel. It was tested at six flight conditions, $q_D = \{60, 100, 163, 207, 281, 343\}$ Pa. At each flight condition, the response to each of the four inputs was tested three times. For the gust vanes, a discrete 4-degree doublet gust was generated with a frequency of 1.45 Hz (approximately equivalent to the first wing bending natural frequency). For the ailerons, a 5-degree frequency sweep from 1 Hz to 2 Hz was performed. For the elevator, a 2-degree frequency sweep from 1 Hz to 2 Hz was performed. This frequency band was chosen as it encompassed the first wing bending mode and also stayed within the bandwidth of the actuators.

The exception to the above is at $q_d = 343$ Pa. At this dynamic pressure, the aileron sweeps were reduced in magnitude to 3.5 degrees and the elevator sweep was reduced in magnitude to 1 degree. This was done in order to reduce the risk of damage to the model due to violent responses at high speeds. <verify with john>

All of these tests were controlled and recorded using Simulink Real-Time. The testing yielded time-series data of input commands and sensor readings for each test.

6.1.1 Data Postprocessing

The time-domain data was post-processed in a similar way as was done for the GVT data in Section 5.2. Each run's data was truncated to start when the input began and end five seconds after the input ended. The data was re-centered to have zero mean and then the three runs of each test were concatenated.

This single concatenated time-domain signal was then buffered into overlapping Hann windows and transformed using the CZT. The FRFs were then computing using Equation 5.1.

6.2 Model Tuning

Chapter 7

RESULTS

Lorem ipsum dolor sit amet, consectetur adipiscing elit. Sed sed erat vehicula elit sollicitudin ultrices at nec ligula. Sed non massa eget nibh pellentesque dapibus non at ante. Integer augue lacus, tincidunt vel sollicitudin fringilla, accumsan vitae lorem. Nunc eleifend scelerisque consectetur. Etiam justo nibh, hendrerit nec mattis non, tincidunt lacinia augue. Morbi ac enim hendrerit, iaculis ante eget, tincidunt massa. Morbi at justo sapien. Donec pulvinar urna id orci sodales, in ornare dolor venenatis. Quisque rutrum mi ac ornare tincidunt.

Sed semper luctus nisi eu tincidunt. Suspendisse gravida sapien libero, et facilisis velit facilisis a. Quisque lorem nisi, viverra a laoreet eu, semper nec nisl. Aliquam ligula lacus, finibus nec sapien et, iaculis pulvinar risus. Suspendisse vitae euismod ligula, vitae porta ipsum. Etiam tellus libero, suscipit id ultrices vitae, vulputate ut risus. Proin ultricies elementum nisi, cursus eleifend velit lacinia nec. Praesent eu quam eu nulla imperdiet varius a ac urna. Suspendisse tristique purus in massa sagittis, vel varius nibh mattis. Donec eget est malesuada, mollis nisl id, dapibus lacus. Aenean aliquam quam in nisl volutpat ultrices.

Sed porta ligula et porttitor lacinia. Aliquam quis nisi vel orci hendrerit lacinia at at risus. Sed condimentum, lectus at elementum facilisis, ante ipsum placerat nibh, eu accumsan metus libero gravida arcu. Aenean et tempus magna, aliquam semper magna. Nulla facilisi. Quisque efficitur dui non lobortis rutrum. Nullam vulputate nec nulla ut suscipit. Nunc et iaculis lacus. Duis aliquam pretium justo, eget finibus sem auctor non. Nulla venenatis ac leo a sodales. In ut rhoncus nibh. Aenean at viverra arcu. Proin accumsan nisl sit amet consectetur pharetra.

Chapter 8

CONCLUSION

Lorem ipsum dolor sit amet, consectetur adipiscing elit. Sed sed erat vehicula elit sollicitudin ultrices at nec ligula. Sed non massa eget nibh pellentesque dapibus non at ante. Integer augue lacus, tincidunt vel sollicitudin fringilla, accumsan vitae lorem. Nunc eleifend scelerisque consectetur. Etiam justo nibh, hendrerit nec mattis non, tincidunt lacinia augue. Morbi ac enim hendrerit, iaculis ante eget, tincidunt massa. Morbi at justo sapien. Donec pulvinar urna id orci sodales, in ornare dolor venenatis. Quisque rutrum mi ac ornare tincidunt.

Sed semper luctus nisi eu tincidunt. Suspendisse gravida sapien libero, et facilisis velit facilisis a. Quisque lorem nisi, viverra a laoreet eu, semper nec nisl. Aliquam ligula lacus, finibus nec sapien et, iaculis pulvinar risus. Suspendisse vitae euismod ligula, vitae porta ipsum. Etiam tellus libero, suscipit id ultrices vitae, vulputate ut risus. Proin ultricies elementum nisi, cursus eleifend velit lacinia nec. Praesent eu quam eu nulla imperdiet varius a ac urna. Suspendisse tristique purus in massa sagittis, vel varius nibh mattis. Donec eget est malesuada, mollis nisl id, dapibus lacus. Aenean aliquam quam in nisl volutpat ultrices.

Sed porta ligula et porttitor lacinia. Aliquam quis nisi vel orci hendrerit lacinia at at risus. Sed condimentum, lectus at elementum facilisis, ante ipsum placerat nibh, eu accumsan metus libero gravida arcu. Aenean et tempus magna, aliquam semper magna. Nulla facilisi. Quisque efficitur dui non lobortis rutrum. Nullam vulputate nec nulla ut suscipit. Nunc et iaculis lacus. Duis aliquam pretium justo, eget finibus sem auctor non. Nulla venenatis ac leo a sodales. In ut rhoncus nibh. Aenean at viverra arcu. Proin accumsan nisl sit amet consectetur pharetra.

BIBLIOGRAPHY

[1] Eli Livne. Aircraft active flutter suppression: State of the art and technology maturation needs. *Journal of Aircraft*, 55(1):410–452, 2018.

[2] William E. Boeing Department of Aeronautics and Astronautics. *3x3 Low-Speed Wind Tunnel*, 2023. `https://www.aa.washington.edu/AERL/3x3` [Accessed: 10/12/2023].

[3] Jake D. Quenzer, Alison Zongolowicz, Kimberly A. Hinson, Bijan Barzgaran, Eli Livne, Mehran Mesbahi, and Kristi Morgansen. *Model for Aeroelastic Response to Gust Excitation*. American Institute of Aeronautics and Astronautics Inc., 2019.

[4] Kenneth L. Roger. Airplane math modeling methods for active control design. In *Structural Aspects of Active Controls*, AGARD-CP-228, Aug 1977.

[5] Siemens. *Aeroelastic Analysis User's Guide*. Siemens Digital Industries Software, 2020.2 edition, 2020.

[6] Theodore Theodorsen. General theory of aerodynamic instability and the mechanism of flutter. Technical Memorandum NACA-TR-496, National Advisory Committee for Aeronautics, Langley Aeronautical Lab. Langley Field, VA, United States, January 1949.

[7] Mark B. Tischler and Robert K. Remple. *Aircraft and Rotorcraft System Identification*, chapter 7. American Institute of Aeronautics and Astronautics, Inc., 1801 Alexander Bell Drive, Reston, VA 20191-4344, 2 edition, 2006.

[8] G.T. Tocklin, J. Crowley, and H. Vold. A comparison of h1, h2, and hv frequency response functions. In *Proceedings of the Third International Modal Analysis Conference*, volume 1, pages 272–278, 1985.

Appendix A

FREQUENCY RESPONSE FUNCTIONS

Magnitude: Wing Bend A

Coherence: Wing Bend A

2012z to 2214z

2012z to 2224z

2012z to 2314z

2012z to 2324z

2020z to 2214z

2020z to 2224z

2020z to 2314z

2020z to 2324z

2214z to 2214z

2214z to 2224z

2214z to 2314z

2214z to 2324z

2224z to 2214z

2224z to 2224z

2224z to 2314z

2224z to 2324z

2314z to 2214z

2314z to 2224z

2314z to 2314z

2314z to 2324z

2324z to 2214z

2324z to 2224z

2324z to 2314z

2324z to 2324z

Frequency (Hz)

Magnitude: Wing Bend B

Coherence: Wing Bend B

Coherence: Fuselage Bend

Magnitude: In-Plane Bend

Coherence: In-Plane Bend

Coherence: Wing Twist